Journal of Materials Research and Technology 37 (2025) 2528–2538

Contents lists available at ScienceDirect

Journal of Materials Research and Technology

journal homepage: www.elsevier.com/locate/jmrt

In situ characterization of phase and microstructural evolution during multi-step heat treatment of an additively manufactured tool steel

Nicole Ofner [a,*], Michael Meindlhumer [a,b], Peter Kunnas [a], Atacan Asci [a], Marek Gocnik [b], Andreas Stark [c], Philipp Höbenreich [d], Christin Aumayr [e], Liang Wu [f], Christoph Turk [e], Jozef Keckes [a], Sabine Carmen Bodner [a]

[a] *Montanuniversität Leoben, Department Materials Science, Leoben, Austria*
[b] *CD Laboratory for Knowledge-based Design of Advanced Steels, Department Materials Science, Leoben, Austria*
[c] *Helmholtz-Zentrum Hereon, Institute of Materials Physics, Geesthacht, Germany*
[d] *Österreichische Akademie der Wissenschaften, Leoben, Austria*
[e] *voestalpine BÖHLER Edelstahl GmbH & Co KG, Kapfenberg, Austria*
[f] *voestalpine Additive Manufacturing Center GmbH, Düsseldorf, Germany*

ARTICLE INFO

Handling editor: P Rios

Keywords:
Tool steels
Additive manufacturing
Post-processing heat treatment
Microstructure evolution
In situ X-ray diffraction

ABSTRACT

Post-printing heat treatment of additively manufactured (AM) tool steels is often essential for optimizing mechanical properties, usually involving complex, multi-step heat treatment procedures. This study investigates the microstructural evolution and its impact on mechanical properties of an AM tool steel through successive heat treatment steps, including the as-built, spheroidized, quenched, sub-zero treated, and three repeated tempered conditions. For the first time, the dynamic mechanisms of phase transformation and carbide evolution during heat treatment of an AM tool steel are systematically revealed through the combined application of *in situ* synchrotron X-ray diffraction and multi-scale characterization techniques. $(Cr,Mo,Mn,V)_{23}C_6$ carbide precipitation was revealed alongside (retained) austenite, martensite and δ-ferrite, with the phase contents varying across the individual heat treatment steps. A strong correlation between (retained) austenite, (tempered) martensite and Vickers hardness was observed, with a final Vickers hardness of 577 ± 5 HV10 in the fully heat-treated condition. Furthermore, the as-built microstructure strongly influenced the subsequent thermal processing behavior as indicated by the stability of δ-ferrite throughout heat treatment, originating from austenite by-passing during LB-PBF, and the early formation of $M_{23}C_6$ carbides during spheroidizing, driven by Cr segregation resulting from the LB-PBF process. Therefore, this study highlights the influence of AM microstructures on heat treatment responses and offers new insights into carbide formation and phase transformations of AM tool steels. The findings emphasize the critical role of post-printing heat treatments in tailoring the microstructural and mechanical properties of tool steels, thus advancing the understanding of specific heat treatment strategies for AM components.

1. Introduction

Tool steels, especially high Cr alloyed martensitic ones, are crucial materials in industries that require components with high hardness, strength and wear resistance [1–3]. Their applications range from cutting and forming tools to molds and dies, where performance is often given by their ability to withstand extreme mechanical and thermal loading conditions [1,3]. Achieving these properties is heavily reliant on the precise control of the material's microstructure, which is generally tailored through well-established heat treatment processes adjusted to the individual steel grade. Conventional heat treatment regimes for tool steels typically consist of austenitization, quenching and multiple tempering cycles [2], often accompanied by prior spheroidizing and intermediate sub-zero treatment [2–5]. Due to the complexity of processes induced during heat treatment, the heat treatment steps must be carefully designed to induce the desired phase transformations and enhance the mechanical and tribological properties of the material.

If applied, spheroidizing as an initial step enhances the material's

---

* Corresponding author.
E-mail address: nicole.ofner@unileoben.ac.at (N. Ofner).

https://doi.org/10.1016/j.jmrt.2025.06.115
Received 15 April 2025; Received in revised form 6 June 2025; Accepted 16 June 2025

workability while promoting microstructural modifications to optimize subsequent processing steps [3]. Austenitization is used subsequently to dissolve carbides at high temperatures and transform the microstructure into austenite, while grain growth should be prevented best possible [2,4]. The subsequent rapid quenching induces the transformation of austenite into martensite in order to maximize hardness [2]. However, this process is accompanied by an increased brittleness of the material and some untransformed (retained) austenite [3,4]. The presence of retained austenite is unwanted, as it may undergo stress-induced phase transformation during service, leading to volumetric expansion that can compromise component dimensional stability and potentially result in premature failure [6]. Sub-zero treatment down to −80 °C is utilized to reduce the retained austenite content by inducing further transformation of austenite to martensite. Subsequent multiple tempering cycles support (i) further austenite-to-martensite transformation, (ii) help to transform tetragonal martensite to cubic martensite, thus enhancing the ductility of the material, and (iii) induce carbide precipitation, improving the material's wear resistance.

As advanced manufacturing methods like additive manufacturing (AM) gain prominence, tool steel production has been redefined. AM offers significant advantages over conventional manufacturing, including near-net-shape production, reduced material waste, and the ability to create complex geometries. However, AM introduces new challenges arising from the multiple thermal cycles inherent to the process, which result in microstructures significantly different from those of conventionally produced tool steels [7–9]. Thus, the as-built microstructure of AM tool steels often deviates from that obtained under equilibrium conditions due to rapid solidification and localized thermal effects [8,10–13]. This deviation can lead to the formation of phases and microstructural features that significantly impact the material's properties. Despite the possibility of *in situ* heat treatments directly during AM, which was studied *e.g.* by Krakhmalev et al. [14], post-processing is often still required. Post-processing of AM parts ranges from the removal of the support structure to machining, finishing and additional heat treatments [15]. As LB-PBF components frequently exhibit suboptimal quality in the as-built state [16] and tool steels are mainly used in their heat-treated condition, the impact of AM on the subsequent heat treatment and the final properties of the component has to be clearly understood. The optimal heat treatment must be adapted not only to the chemical composition of the steel but also to its initial microstructure, which is directly influenced by the manufacturing process [17].

While conventional tool steels have been extensively studied, research on AM tool steels is still emerging, particularly concerning post-processing heat treatment. The unique as-built microstructures generated by AM [10,18,19] – *e.g.* higher inhomogeneity as a result of local variations of the energy input due to the layer-wise built-up and visible laser tracks and melt pools – necessitate a re-evaluation of conventional heat treatment strategies, as the traditional approaches may not be directly applicable. The high Cr content in the studied AM tool steel adds another layer of complexity, influencing the formation and stability of phases such as δ-ferrite, martensite, and austenite, as well as carbide precipitation [11]. Due to process-specific characteristics in AM differences in the initial microstructure prior to heat treatment between AM tool steels and conventionally produces ones arise *e.g.* in elemental segregations, phase formations, grain sizes and residual stresses [20]. Carbide formation may be suppressed during rapid solidification, leading to altered carbide size, shape, distribution, and dissolution behavior during subsequent heat treatment [20,21]. Furthermore, phase fractions and types present before heat treatment [20] – such as retained austenite or δ-ferrite – can differ, affecting transformation behavior and diffusion kinetics during heat treatment [17]. These differences in the initial microstructures of AM materials compared to conventionally produced ones are expected to influence the heat treatment response and properties after heat treatment fundamentally [20,22], yet systematic investigations comparing AM and conventionally processed materials remain sparse [21].

Existing studies have primarily focused on other materials [16,20,21] or on the characterization of steels in the as-built condition and the condition after the final heat treatment [5,17,23–34], often neglecting the transformations occurring during individual heat treatment steps. Most of these studies focus on AM processed tool steels such as H13 [5,6,29,32] and 17-4 PH [24,27,28]. Among others, studies by Cheruvathur et al. [24] and Vahedi Nemani et al. [25] demonstrated that post-printing heat treatments reduce the heterogeneity of the AM microstructure. However, to date, a systematic investigation of phase transformations and carbide evolution throughout each heat treatment step in AM high Cr alloyed tool steels remains lacking.

Therefore, this study addresses this gap by systematically analyzing the effects of each step in a conventional heat treatment regime on the microstructural evolution and phase occurrences of an AM high Cr alloyed martensitic tool steel. These steps include spheroidizing, austenitization and quenching, sub-zero treatment and multiple tempering cycles. The quantitative phase evolution over the entire heat treatment was investigated for the first time using *in situ* synchrotron X-ray diffraction (XRD) combined with dilatometry to gain deep insights into the thermal evolution of the material's properties. Additional *ex situ* methods involved scanning electron microscopy (SEM) combined with electron backscatter diffraction (EBSD), scanning transmission electron microscopy (STEM) coupled with energy dispersive X-ray spectroscopy (EDS), and Vickers hardness measurements in the as-built condition as well as in the condition after every step of the heat treatment. The results indicate that the microstructural and phase characteristics imparted by the AM process necessitate the development of tailored heat treatment regimes specifically adapted to AM-produced components. Thus, this study contributes to the growing body of knowledge on post-processing heat treatment strategies for AM tool steels to gain optimal performance in industrial applications.

2. Materials and methods

2.1. Material

A gas-atomized tool steel powder, supplied by voestalpine Böhler Edelstahl GmbH & Co KG, was additively manufactured using laser beam powder bed fusion (LB-PBF) in an Ar atmosphere at a volumetric energy density of 58 J/mm^3 in an Aconity MIDI + metal printer (Aconity3D GmbH. Herzogenrath, Germany). Laser power, scan speed, hatch distance and layer thickness were set to 214 W, 928 mm/s, 0.1 mm and 0.04 mm, respectively. Furthermore, a platform preheating temperature of 200 °C and a stripe hatching strategy with a stripe width of 10 mm were applied. The AM tool steel achieved a relative density of >99.95 %. The martensite start temperature M_s of the alloy was determined to be 124 °C through previous laboratory dilatometry experiments (Suppl. Fig. 1). The chemical composition of the tool steel powder and the corresponding AM alloy are identical and given in Table 1.

2.2. Sample preparation

First, the AM tool steel was sectioned into seven identical samples

Table 1
Chemical composition of the investigated tool steel powder and the corresponding AM tool steel [wt.%].

alloying elements	C + N	Si	Mn	Cr	Mo	V	Ni	Fe
Composition range of the tool steel powder [wt.%]	0.7	0.3	0.3	19–20	1.2	0.1	0.8	bal.
Composition range of the AM tool steel [wt.%]	0.7	0.3	0.3	19–20	1.2	0.1	0.8	bal.

using electric discharge machining (EDM). This procedure ensured identical starting conditions for all seven samples cut from the parent AM tool steel prior to heat treatment (*cf.* Sec. 2.3). Sample 1 to 6 were characterized in terms of microstructure and mechanical properties after their final heat treatment step (*cf.* Table 2 and Fig. 1), whereas Sample 7 was additionally also analyzed *in situ* during the single heat treatment steps (except sub-zero treatment). To clearly specify the heat treatment steps applied to each sample, their final conditions during characterization and characterization methods conducted, as well as the corresponding terminology used throughout the paper, an overview is provided in Table 2. The single heat treatment steps are described in detail in Sec. 2.3 and Fig. 1.

For *ex situ* microstructural analyses, metallurgical cross-sections and STEM samples were prepared from each sample (sample 1 to 7). The metallurgical cross-sections were prepared in a three-step sequence: first, the samples were hot embedded at 180 °C for 15 min in a Polyfast phenol resin (Struers GmbH, Willich, Germany); second, they were manually grinded to be polished in a third step. Polishing was conducted using following polishing suspensions: Struers' DiaPro Allegro/Largo suspension (9 μm), Struers' DiaPro Dac suspension (3 μm), and QPrep's Chem. Eposil Non-Dry suspension (0.05 μm).

For STEM, small discs (Ø3 × 0.1 mm^2) were first extracted from the as-built and each heat-treated condition (sample 1 to 7) by EDM cutting and then mechanically polished. Next, the STEM samples were electrochemically polished at 12 °C in a TenuPol-5 (Struers GmbH, Willich, Germany) to achieve electron transmission. The used electrolyte was a mixture of acetic acid and perchloric acid. Voltage and current were set to 70.0 V and 190–225 mA, respectively, for a duration of 25–45 s.

2.3. *In situ synchrotron XRD coupled with dilatometry*

As tool steels are primarily used after heat treatment, the AM martensitic Cr tool steel underwent a multi-step heat treatment, plotted in Fig. 1, compromising six steps: (i) spheroidizing, (ii) austenitization followed by quenching, (iii) sub-zero treatment and (iv) three tempering cycles. Each of the seven samples underwent the heat treatment steps described in Table 2 and plotted in Fig. 1. As the samples were cut from the same AM tool steel prior to heat treatment, they will be further referred to by their (heat-treated) condition.

In detail, starting from the as-built condition, spheroidizing was conducted as a first heat treatment step at 800 °C for 3 h with a heating and cooling rate of 3 K/s. Austenitization was carried out at 1050 °C for 30 min with the same heating rate, followed by gas quenching at a cooling rate of 40 K/s. Due to limitations in the dilatometer setup, sub-zero treatment was conducted *ex situ* at −80 °C for 2 h. Finally, after sub-zero treatment, the martensitic Cr steel underwent three tempering cycles at 490 °C for 2 h each, with heating and cooling rates of 3 K/s for each cycle.

Table 2
Overview of sample designations, applied heat treatment steps, performed characterizations, and final conditions referred to in this study. The heat treatment steps given here are detailed in Fig. 1.

Sample	heat treatment steps	performed characterization	final condition/ further referred to as
1	1	Microstructural characterization + mechanical properties	as-built
2	1 + 2	Microstructural characterization + mechanical properties	Spheroidized
3	1 to 3	Microstructural characterization + mechanical properties	Quenched
4	1 to 4	Microstructural characterization + mechanical properties	Sub-zero treated
5	1 to 5	Microstructural characterization + mechanical properties	1 × tempered
6	1 to 6	Microstructural characterization + mechanical properties	2 × tempered
7	1 to 7	*in situ* X-ray diffraction + microstructural characterization + mechanical properties	3 × tempered

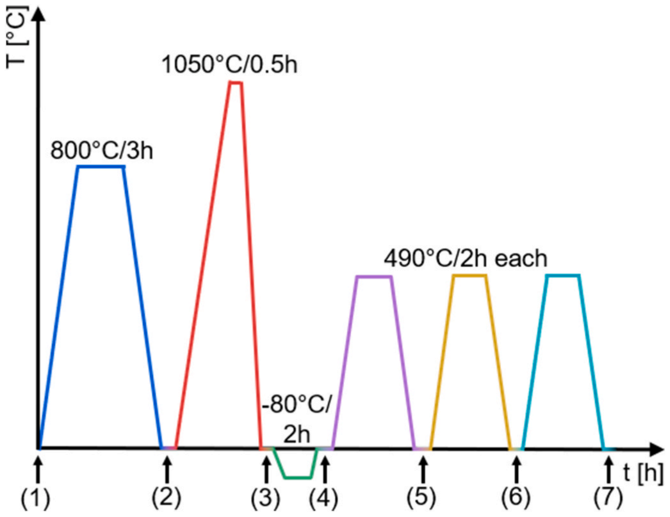

Fig. 1. Heat treatment regime for the AM martensitic Cr tool steel. Starting from the as-built (1) condition, the tool steel was spheroidized (2), quenched (3), sub-zero treated (4) and three times tempered (5–7). Thus, sample 1 remained in the as-built condition (heat treatment step 1), sample 2 was spheroidized (step 2), sample 3 additionally quenched (step 3), sample 4 moreover sub-zero treated (step 4), sample 5 1 × tempered in addition (step 5), sample 6 additionally 2 × tempered (step 6) and sample 7 fully heat-treated compromising another third tempering step (step 7). The samples are further referred to solely by their (heat-treated) condition.

All heat treatment steps, except sub-zero treatment, of sample 7 were performed *in situ* during a synchrotron experiment at the 'High Energy Materials Science' (HEMS) beamline P07B, operated by Hereon, of the PETRA III storage ring at DESY in Hamburg. The sample was heated in a vacuum environment and cooled down by Ar in a DIL 805 dilatometer (TA Instruments, Eschborn, Germany). To investigate the phase transformation behavior during each heat treatment step (Fig. 1), the sample was characterized by XRD using an X-ray beam with an energy of 87.1 keV in transmission diffraction geometry. The distance between sample and detector was ~1.15 m and LaB_6 powder was used as a calibrant. A two-dimensional (2D) flat-panel detector (PerkinElmer, Inc., Waltham, USA) with a pixel matrix of 2048 × 2048 pixels at a pitch of 200 μm was used to capture the diffraction patterns. During the performed heating experiments, the time resolution was approximately 7.5 s, i.e. every 7.5 s a diffraction pattern was recorded. The used exposure time was 0.2 s, with a similar detector dead time. The collected synchrotron XRD data was further analyzed with the Python-based software package "PyFAI" [35]. The XRD data was thus radially integrated in segments in a range of $3^\circ < 2\theta < 9.5^\circ$. The software "Profex" (version 5.3) [36] was used to evaluate the type and fraction of occurring phases at the beginning and the end of each heat treatment step by Rietveld refinement.

2.4. *Microstructural characterization*

Optical microscopy of the as-built and each heat-treated condition was performed on an Olympus BX51 microscope (Olympus Corporation, Tokyo, Japan) in order to evaluate porosity and on an Axio Imager.M1 microscope (Carl Zeiss AG, Oberkochen, Germany) to analyze the microstructure after Beraha etching [37].

SEM and EBSD analyses of each condition were conducted in the unetched condition on a Tescan Magna SEM (Tescan Group, Brno, Czech Republic), equipped with a backscattered electron (BSE) detector for imaging and an eFlash FS EBSD detector (Bruker Corporation, Billerica, USA). Operating conditions included a beam current of 10 nA and an acceleration voltage of 20 keV, with the electron backscatter patterns captured at a resolution of 160 × 120 pixels and an exposure time of 11–12 ms.

For detailed microstructural characterization and carbide analysis of the as-built and each heat-treated condition, a JEOL-2200FS S/TEM (JEOL Ltd., Tokyo, Japan) with an integrated EDS detector was used at an acceleration voltage of 200 kV. Bright field (BF) micrographs were acquired to examine the microstructure in each heat treatment step in unetched condition and the microstructural characterization was performed using a 40 μm condenser lens aperture (CLA) inserted and a nominal probe size of 0.7 nm. For the EDS elemental mapping 40 μm or 100 μm CLA was inserted and either 0.7 or 1.5 nm nominal probe size was selected to optimize the X-ray counts at the detector. Post-processing of the elemental maps, including signal normalization and background adjustment, was carried out using version 5.0 of the AZtecTEM software (Oxford Instruments, High Wycombe, UK).

2.5. *Mechanical properties*

The mechanical properties of the as-built and each heat-treated condition were evaluated by Vickers hardness measurements conducted on a DuraScan microhardness testing machine (ZwickRoell AG, Ulm, Germany). Measurements were performed in a 3 × 3 grid pattern across the parts' cross-sections, applying a load of 10 kp (HV10) according to ASTM E384. Individual indents were placed at least 1 mm away from the sample's edges and the same distance was kept between other measurement points. In this way, a mean hardness value and the standard deviation over nine indents were calculated for each heat treatment step.

3. Results and discussion

The results of the microstructural and mechanical characterizations after particular heat treatment steps – including as-built (1), spheroidized (2), quenched (3), sub-zero treated (4), 1 × tempered (5), 2 × tempered (6), and 3 × tempered (7) conditions – are presented and discussed in Secs. 3.1–3.3. In Figs. 2–4, the *in situ* phase characterization is shown for the spheroidizing ((1) to (2)), the austenitization and quenching ((3) to (4)) and the tempering steps ((5 to (7)), respectively. Additionally, Fig. 5 presents intensity vs. 2*θ* plots in conjunction with the corresponding quantitative phase analysis for each condition.

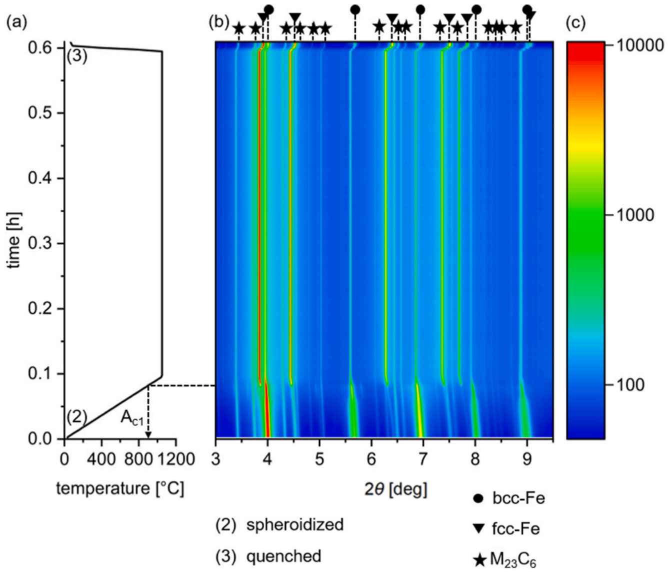

Fig. 3. Phase evolution of the AM tool steel (sample 7) during austenitization at 1050 °C for 30 min followed by gas quenching. During this heat treatment step, the sample transitions from the spheroidized (2) to the quenched (3) condition. The temperature profile during this heat treatment step is shown in (a). The evolution of the detected phases is presented in the phase–temperature contour plot in (b), where the intensity of the diffraction peaks is shown on a color scale in arbitrary units in (c).

3.1. *In situ synchrotron X-ray diffraction*

3.1.1. *Spheroidizing*

In situ synchrotron XRD was employed to monitor the heat treatment steps of an AM martensitic tool steel, starting from the as-built condition. Initially, spheroidizing was conducted to track the evolution of phases throughout the temperature program, as illustrated in Fig. 2.

In the as-built condition, the primary phase present is face-centered cubic (fcc)-Fe, which corresponds to (metastable) austenite and is represented by the highest intensity in arbitrary units (*cf*. Fig. 2). Additionally, a minor amount of body-centered cubic (bcc)-Fe phase, previously identified as δ-ferrite for the identical steel and process

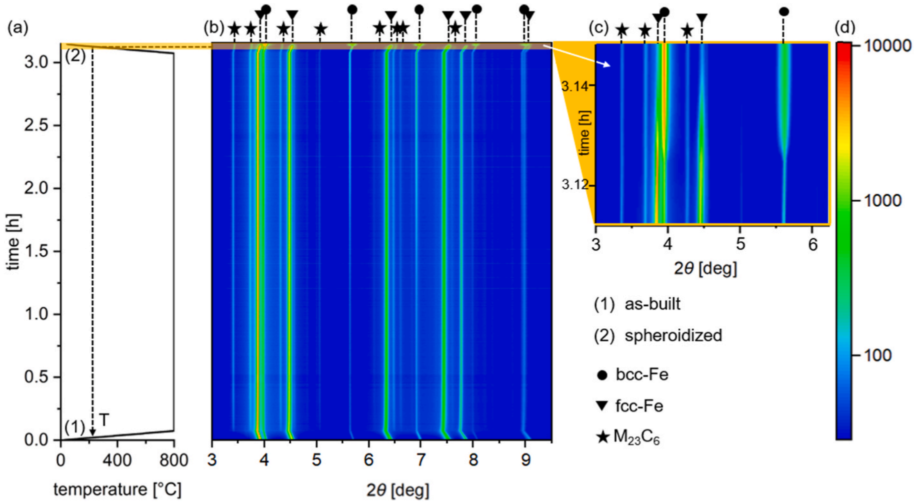

Fig. 2. Phase evolution of the AM tool steel (sample 7) during spheroidizing at 800 °C for 3 h. During this heat treatment step, the sample transitions from the as-built (1) to the spheroidized (2) condition. The temperature profile during spheroidizing is shown in (a), while the evolution of the detected phases is presented in the phase–temperature contour plot in (b). A detailed representation of the phase transformation during the last 130 s of cooling down to room temperature (marked in yellow) at the transition temperature T (~240 °C) is shown in (c). The color scale in (d) gives the intensity of the diffraction peaks in arbitrary units and is valid for (b) and (c), respectively.

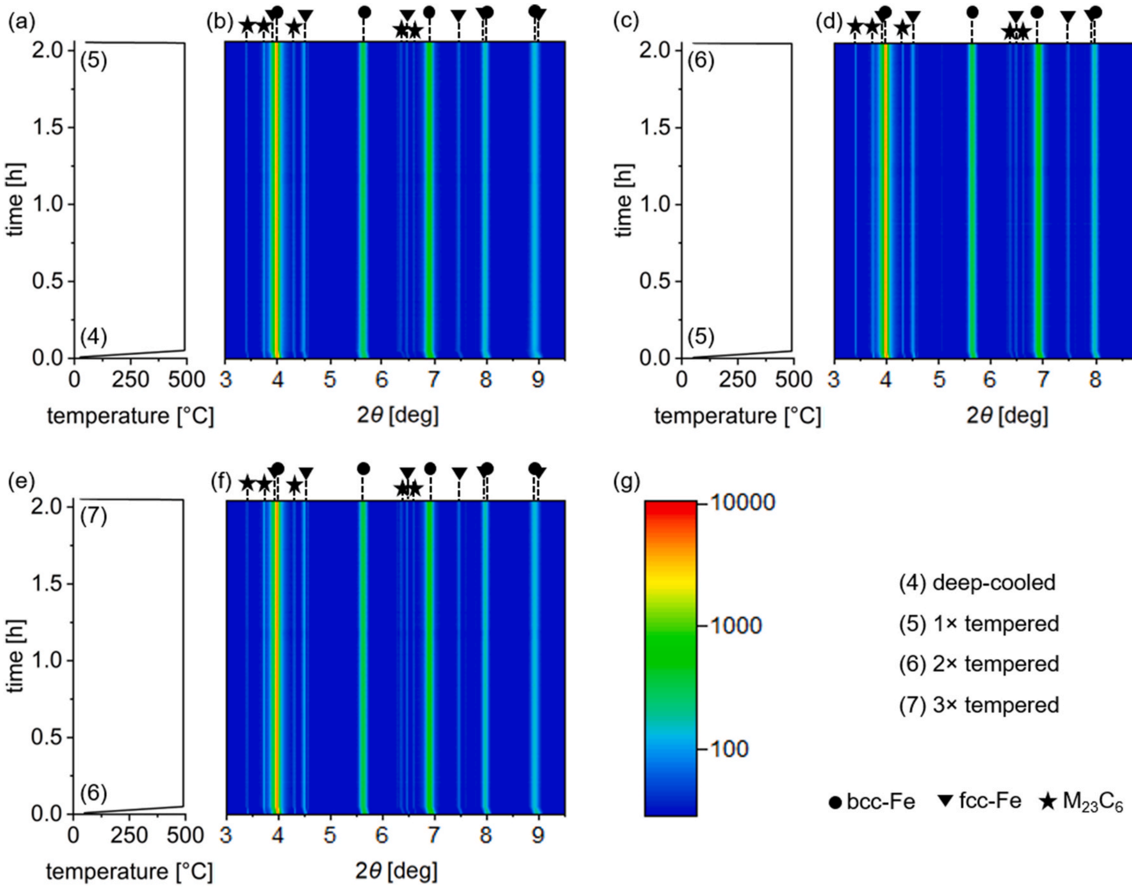

Fig. 4. Phase evolution of the AM tool steel (sample 7) during the first (a,b), second (c,d) and third (e,f) tempering step at 490 °C for 2 h each. During these heat treatment steps, the sample transitions first (a,b) from the sub-zero treated to the 1 × tempered condition, second (c,d) from the 1 × to the 2 × tempered condition and third (e,f) from the 2 × to the 3 × tempered and thus fully heat-treated condition. The temperature profiles during the individual tempering steps are shown in (a, c,e), while the evolution of the detected phases during the single tempering steps are presented in the phase–temperature contour plots in (b,d,e). The color scale in (g) indicates the intensity of the diffraction peaks in arbitrary units and applies for (b), (d) and (f), respectively.

conditions [11], is observed. This δ-ferrite is stabilized down to room temperature due to the high Cr content of the tool steel, combined with the rapid solidification and cooling rates characteristic of the LB-PBF process [17,38,39]. The mechanism underlying δ-ferrite stability was studied in detail in a previous study by Ofner et al. [11], demonstrating – supported by findings from literature [7,8,17,39,40] – that in high Cr alloyed tool steels the high Cr content, as Cr is a strong ferrite stabilizer, and the high solidification and cooling rates of AM, which may result in by-passing of the austenitic phase, are key driving factors for the stability of δ-ferrite.

No carbides are detected in the as-built condition, indicating that carbide formation does not occur during the printing process but is exclusively achieved through subsequent heat treatment. The absence of carbides directly after the AM process is also attributed to the high solidification and cooling rates during AM [30], which suppress the diffusion kinetics necessary for carbide nucleation and growth [17].

During heating up to holding temperature, a slight peak shift is observed in all phases. This peak shift is best visible for the fcc-Fe peak, since fcc-Fe has the highest coefficient of thermal expansion ($\alpha_{\text{fcc-Fe}} \sim 2.2 \times 10^{-5}$ °C^{-1}) approximately 50 % higher compared to the thermal expansion coefficient of bcc-Fe ($\alpha_{\text{bcc-Fe}} \sim 1.5 \times 10^{-5}$ °C^{-1}) during heating [41]. Carbide formation is first observed at the beginning of the holding segment during spheroidizing at 800 °C (Fig. 2). During the holding period of 3 h, the highly alloyed, metastable austenite resulting from the AM process decomposes into (comparably) lower-alloyed austenite and carbides, supported by the formation of $M_{23}C_6$-type carbides as identified by the X-ray analysis (Fig. 2) [42]. These carbides persist throughout the spheroidizing step and align well with predictions from Thermo-Calc calculations (*cf.* Suppl. Fig. 2). Additionally, the bcc-Fe phase content increases slightly during the holding period, which may be attributed to the reduction of C content in the matrix, as C, a known austenite-stabilizing element [43], is reduced in the matrix due to carbide formation.

During the last 130 s of cooling down to room temperature at a cooling rate of 3 K/s (Fig. 2c), a sharp increase in the bcc peak intensities and significant peak broadening are observed. The transition temperature is crossed at approximately 240 °C, resulting in a phase transformation from austenite (fcc-Fe) to martensite. This martensite exhibits a body-centered tetragonal (bct) crystal structure; however, due to the minimal tetragonal distortion of the martensitic cell [44], the software classifies the bct martensite as bcc-Fe. Peak shift and peak broadening at the end of the spheroidizing step indicate (i) contraction of the crystal lattice due to cooling, (ii) the development of second- and third-order strains associated with martensite formation and (iii) peak overlap arising from the coexistence of bcc and bct phases. A fraction of the bcc-Fe phase is expected to remain as δ-ferrite, as the spheroidizing temperature of 800 °C is insufficient to drive a complete δ-ferrite--to-austenite transformation, given that in high Cr alloyed Fe–Cr–Ni systems, δ-ferrite and austenite can coexist up to 1300 °C [45].

3.1.2. *Austenitization and quenching to room temperature*

Subsequent to the spheroidizing step, an austenitization treatment at 1050 °C for 30 min followed by gas quenching was performed. The phase evolution during austenitization and quenching is presented in the

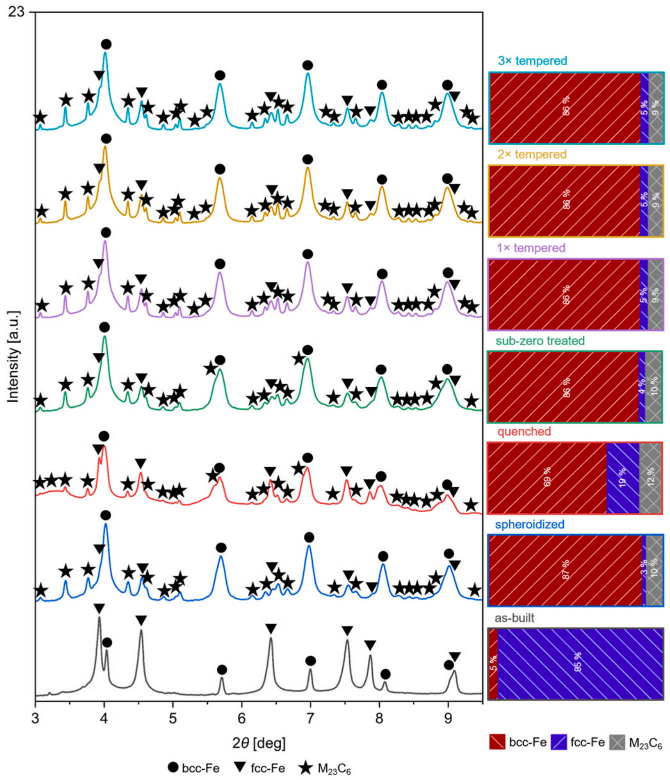

Fig. 5. Overview of selected X-ray diffractograms corresponding to each heat treatment step (left). Relative phase fractions of bcc-Fe, fcc-Fe, and $M_{23}C_6$ carbides for the as-built condition and each heat-treated condition were evaluated by Rietveld refinement and are shown on the right. In contrast to the contour phase plots shown in Figs. 2–4, Fig. 5 displays individual diffractograms, allowing weaker carbide peaks – often obscured by the proximity to intense fcc- and bcc-Fe peaks – to be more distinctly identified.

contour plot in Fig. 3.

Since austenitization and quenching were performed directly after the spheroidizing step, the initial phase appearance at the bottom in Fig. 3 is identical to the one presented at the upper end of Fig. 2. The composition consists predominantly of martensite, accompanied by small amounts of fcc-Fe (retained austenite) and $M_{23}C_6$ carbides as well as δ-ferrite, which did not transform during spheroidizing. However, the latter cannot be distinguished from the martensite alone by the XRD phase analysis as discussed above. During heating up, a transition from bcc-Fe (martensite + ferrite) to fcc-Fe (austenite) peaks is observed, allowing the determination of the A_{c1} temperature of ~890 °C (*cf.* Fig. 2). The spheroidizing temperature should be close to the A_{c1} temperature [46], which was confirmed by the A_{c1} temperature of ~890 °C. Between ~700 and ~975 °C, metastable martensite transforms into α-ferrite, as evidenced by the intensity increase and the reduced peak broadening of the 200 peak at 2θ of ~5.6° in this temperature range. Simultaneously, new peaks appear in this temperature range, which could be identified as Fe_3C carbide precipitation due to the decomposition of martensite into α-ferrite and Fe_3C (Fig. 3b). During further phase transformation from α-ferrite to austenite at a temperature of ~975 °C, the Fe_3C carbides dissolve into the fcc-Fe matrix, given the significantly higher solubility of C in the fcc-Fe [47].

During austenitization at 1050 °C nearly all of the bcc-Fe phase is transformed into austenite (*cf.* holding period in Fig. 3b). The observed phase composition aligns with the Schaeffler diagram's predictions for this alloy composition [48] and prior Thermo-Calc simulations (*cf.* Suppl. Fig. 2). Above the A_{c1} temperature, α-ferrite and martensite start to transform into austenite, while δ-ferrite remains stable until higher temperatures. Consequently in alignment with the literature [11], the bcc-Fe phase persisting until the end of the holding time is attributed solely to δ-ferrite.

A Rietveld analysis of the diffractograms recorded at the end of the holding time before quenching – this is a state where no martensite phase, but only δ-ferrite is stable as bcc-Fe phase – revealed that δ-ferrite accounts for approximately 6 % of the phase composition. This indicated minimal change in δ-ferrite content from the as-built condition onwards. Studies on other steels, such as 420 martensitic stainless steel conducted by Vahedi Nemani et al. [17], demonstrate the successful removal of δ-ferrite at 1150 °C, highlighting different optimal austenitization conditions for AM steels compared to conventionally produced ones. However, the austenitization temperature of 1050 °C and/or time of 30 min used in this study were insufficient to achieve full δ-ferrite-to-austenite transformation [11]. Nevertheless, since higher austenitization temperatures are known to promote grain growth – which can be detrimental to the mechanical properties after heat treatment – this effect was mitigated by applying an austenitization temperature below 1080 °C [49].

The analysis of the synchrotron XRD data revealed an increased presence of $M_{23}C_6$ carbide peaks during austenitization and quenching compared to the spheroidized condition. This indicates a comparatively higher concentration of carbides. In contrast to Fe_3C described before, $M_{23}C_6$ carbides are already formed during spheroidizing and persist throughout the austenitization step – *i.e.* they do not dissolve into the matrix and reform during tempering. This behavior is in contrast with findings by Barlow et al. [4], where $M_{23}C_6$ carbide dissolution between 950 and 1050 °C is reported for the conventionally produced martensitic stainless steel AISI 420. The persistent presence of carbides throughout austenitization (*cf.* Fig. 3) may result from the metastable AM microstructure and elemental segregations, leading to carbide formation and stabilization during spheroidizing and austenitization. Pellizzari et al. [22], among others, highlighted the impact of the initial solidification structure – corresponding to the AM one in the present study – on the microstructure, and thus also phase occurrence, after applying a heat treatment regime.

During quenching to room temperature, an increase in bcc-Fe phase is observed, accompanied by peak broadening indicative of martensite formation (Fig. 3b). Due to the very high cooling rate, a determination of M_s was not possible in this case. The final transition from austenite (fcc-Fe) to martensite (counted as bcc-Fe) is thus best visible in the single X-ray diffractogram evaluated at the end of the quenching experiment, described in Sec. 3.1.4 (Fig. 5). Higher cooling rates may be necessary to enhance a full transformation from austenite to martensite. However, heat treatment of the same tool steel under undefined, industrial conditions resulted in a similar bcc-Fe phase content of 73 % after quenching (*cf.* Suppl. Table 1).

3.1.3. *Sub-zero treatment and tempering*

The sub-zero step was performed *ex situ* due to equipment constraints of the dilatometer, but both pre- and post-sub-zero treated conditions of the material were characterized using synchrotron XRD. The tempering steps were again observed by *in situ* synchrotron XRD coupled with dilatometry, the corresponding phase evolution is shown in Fig. 4.

Broad bcc-Fe peaks remain present during each tempering step indicating martensite presence. Typically, during tempering, bct martensite transforms into bcc martensite [50]. Additionally, weak fcc-Fe peaks and $M_{23}C_6$ carbide peaks are observed. However, there is a negligible change of the diffraction peaks during tempering.

3.1.4. *Summary of the quantitative phase analysis*

The overall changes in the diffraction peaks and quantitative phase analyses across the heat treatment steps are shown in Fig. 5. Due to low carbide peak intensities and the proximity to stronger peaks (fcc-Fe and bcc-Fe), fewer carbide peaks are visible in the contour phase plots (*cf.* Figs. 2–4) than in the individual diffractograms presented in Fig. 5. To ensure the reliability of the XRD results presented in Fig. 5, the Rietveld refinement was conducted applying the same experimental setup parameters as employed during the *in situ* synchrotron XRD measurements. This approach enabled a direct correlation between refinement outputs and experimental conditions, ensuring accurate identification of phase types and their corresponding fractions. The quality of the fit was verified by visually comparing the observed and calculated patterns, and by ensuring that the refinement model accurately reflected the experimental configuration – an essential criterion for Rietveld analysis quality, as outlined in Ref. [51]. Additionally, the phase fraction results, particularly in the as-built and fully tempered conditions, were in good agreement with data from SEM-EDX and EBSD analyses reported in previous studies [11,13].

The as-built condition primarily consists of fcc-Fe phase (austenite) with some bcc-Fe (identified as δ-ferrite in agreement with [11]). After spheroidizing, the bcc-Fe phase (mainly martensite with some δ-ferrite) was the predominant phase, along with some fcc-Fe phase (retained austenite) and $M_{23}C_6$ carbides. The bcc-Fe phase was also the predominant phase after quenching. However, the retained austenite content (~19 % fcc-Fe phase) was higher compared to spheroidizing. This phenomenon arises from the stabilization of the austenitic phase during austenitization, resulting in a very stable austenite. Sub-zero treatment was used to further transform retained austenite into martensite [5] resulting in a reduced fcc-Fe phase (retained austenite) content of ~4 %. The further presence of retained austenite indicates that the martensite finish temperature M_f of the investigated tool steel is below −80 °C. The content of retained austenite increases slightly from 4 % to 5 % during tempering. Krakhmalev et al. [14] found that multiple thermal cycling between M_s and A_{c1}, like the used tempering temperature of 490 °C, can initiate C diffusion. The C atoms are expected to migrate to grain boundaries and dislocations [17], leading to austenite stabilization and an increased amount of retained austenite or austenite reversion [14]. Reverted austenite formation during tempering has not clearly been understood yet [52]. It is usually associated with maraging steels [53], but was also reported by Niessen et al. [54] for the heat-treated super-martensitic stainless steel X4CrNiMo16-5-1. Nevertheless, the slight increase of austenite content during tempering may also be attributed to measurement inaccuracy, as ~1 % is expected as the potential error in terms of Rietveld refinement [55].

The carbide content increases from the as-built (0 %) to the spheroidized (10 %) and quenched (12 %) condition, followed by 10 % carbides in the sub-zero treated condition. This decrease in carbide content is likely due to $M_{23}C_6$ carbides counted as bcc-Fe as some $M_{23}C_6$ peaks are very close to the stronger bcc-Fe peaks (*cf.* Fig. 5). Minimal changes in $M_{23}C_6$ carbide quantity were measured from sub-zero treated (10 %) to the tempered (9 %) conditions.

3.2. Microstructural analysis

The microstructural evolution after each heat treatment step was analyzed using SEM and EBSD. Results are provided in the supplementary material (Suppl. Figs. 3 and 4). In the as-built condition, the AM microstructure consists mainly of columnar grains with a lower density of grain boundaries compared to all heat-treated conditions (*cf.* Suppl. Fig. 3–1a). In the as-built microstructure, no cracks were observed. Additionally, no keyhole pores or lack-of-fusion defects were detected, indicating that hot isostatic pressing (HIP) is unnecessary as a post-processing step [29].

The microstructure is refined from the as-built to the fully heat-treated condition (Table 3). The average grain size is the smallest for the quenched and sub-zero treated condition, which is in agreement with the presence of fine-grained bct martensite. During tempering there is a slight increase in grain size, which may be attributed to (i) bct to bcc martensite transformation, (ii) carbide growth, and/or (iii) detection area.

The presence of carbides is evident from the spheroidized condition onwards until the end of tempering (*cf.* Suppl. Figs. 3 and 4).

EBSD measurements further confirm that the fcc-Fe phase (austenite) is the main phase in the as-built condition, with a minor bcc-Fe phase fraction of 7 % (*cf.* Suppl. Fig. 3–1c), identified as δ-ferrite in previous works on this material [11,13]. In the spheroidized condition, the microstructure changes to predominantly bcc-Fe, consisting mainly of martensite and a small proportion of persistent δ-ferrite, and experienced grain refinement. Despite this effect, the scan paths from LB-PBF are still visible (*cf.* Suppl. Fig. 5a). These scan paths, characteristic of layer-wise AM techniques, were fully eliminated only after austenitization and quenching (*cf.* Suppl. Fig. 5b), consistent with findings from other studies [31,32,42,56].

After the next heat treatment step, which consists of austenitization and quenching, retained austenite (fcc-Fe), martensite and δ-ferrite (both counted as bcc-Fe) are found in the microstructure. A sub-zero treatment and subsequent tempering led to a microstructure with a high content of bcc-Fe, mainly represented by martensite. The δ-ferrite content is expected to be constant, as described in Sec. 3.1.2 and in Ref. [11]. However, accurate phase quantification via EBSD was challenging due to the very fine microstructure which goes hand in hand with an increased grain boundary density and led to high zero-solution values and errors in nominal phase identification. Additionally, carbides were either classified as zero solutions or incorrectly attributed to the bcc-Fe phase. Consequently, the phase fractions determined by XRD offer more reliable data for quantitative phase analysis in the context of this study.

To perform a detailed analysis of the sample microstructures after every heating step, STEM was employed. STEM-EDS analysis was used to identify the carbide type(s) and the elements involved in carbide formation. BF STEM and STEM-EDS images for all heat treatment steps are presented in Fig. 6.

In the as-built condition, the microstructure is characterized by globular cells with elemental segregations along subgrain boundaries. Specifically, Fe depletion and Cr enrichment (Figs. 6–1b,c) can be determined. However, no C enrichment was detected in Figs. 6–1d, indicating that carbide formation does not occur during AM. This observation aligns with the phase analysis presented in Sec. 3.1. The determined elemental segregations are typical for AM-produced microstructures [7,10,57,58] and often necessitate post-processing heat treatments to homogenize the composition, even when the alloy's composition nominally meets the specification of the data sheet [27]. In STEM images of the following heat-treated conditions, martensite laths are visible (*cf.* Figs. 6–3a to 7a), without any further elemental segregations, except for $M_{23}C_6$ carbide formation.

During the spheroidizing step, the elements rearranged and formed homogeneously distributed carbide networks, still accompanied by Fe depletion and now enrichments of Cr and C, as seen in Figs. 6–2c. Therefore, Cr segregation in the as-built microstructure, induced by the LB-PBF process, appears to facilitate early carbide formation during spheroidizing. These networks are split up into individual carbides by the end of quenching. Similarly, Vilardell et al. [26] reported that the carbide networks fragmented into randomly dispersed carbides during austenitization, in that case for a modified X33CrMoNiW 3–2 hot-work

Table 3
Grain sizes of the as-built condition and the individual heat treatment steps, measured according to EBSD data.

condition	as-built	spheroidized	quenched	sub-zero treated	1 × tempered	2 × tempered	3 × tempered
Average grain size [μm]	5.6	1.9	1.1	1.1	1.5	1.8	1.2
Median grain size [μm]	3.5	1.2	0.9	0.7	1.1	1.1	0.87

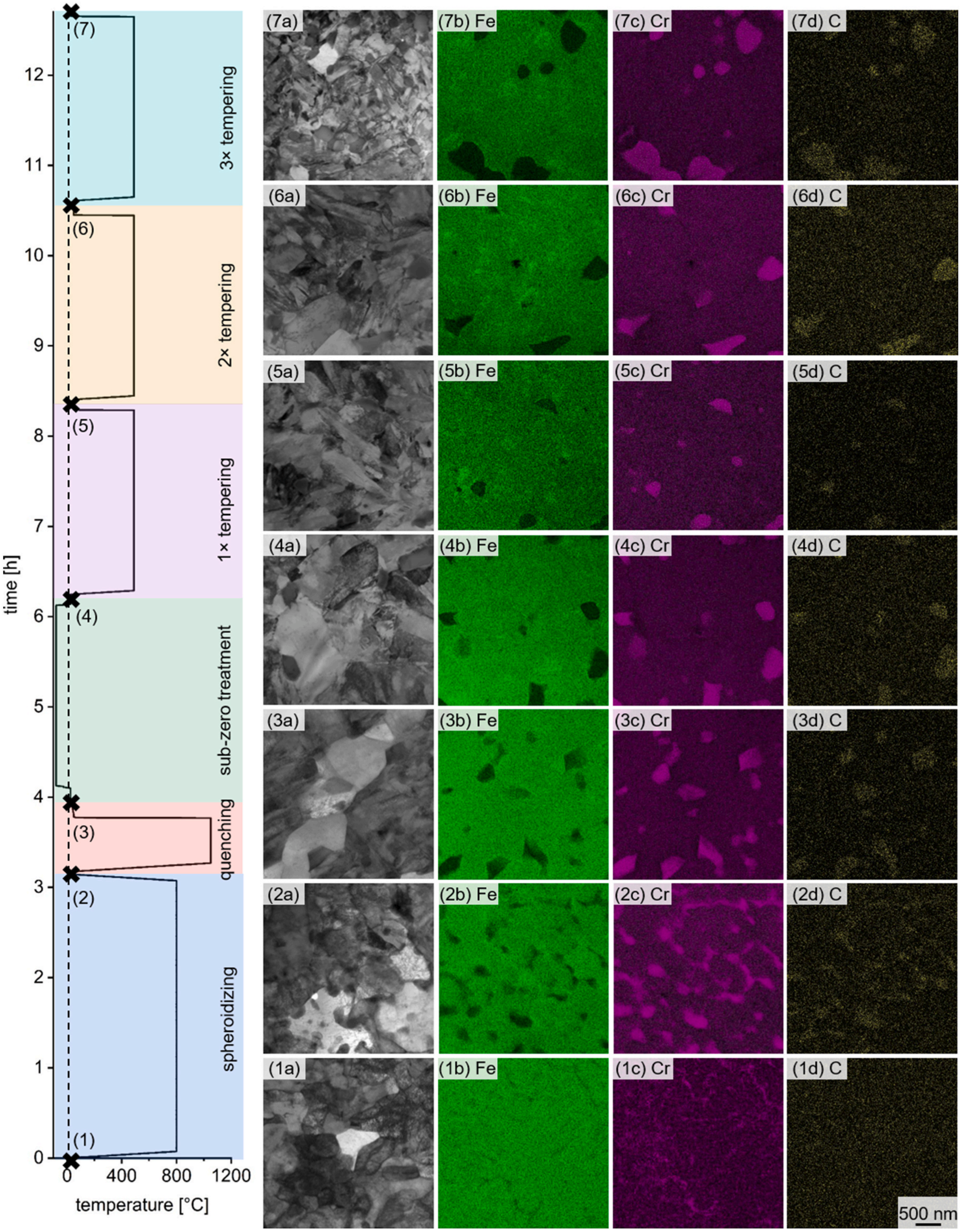

Fig. 6. (a) BF STEM images and (b–d) corresponding EDS maps for Fe, Cr, and C, respectively, across various heat treatment conditions: as-built (1), spheroidized (2), quenched (3), sub-zero treated (4), 1 × tempered (5), 2 × tempered (6), and 3 × tempered (7). The total heat treatment scheme applied on the AM tool steel is shown on the left side of the image. The scale bar in (1d) applies to all images.

tool steel processed through LB-PBF and heat-treated with an austenitization temperature of 1020 °C.

Carbides were observed to precipitate along prior austenite grain and subgrain boundaries [59,60] and did not dissolve during austenitization. This behavior can potentially be attributed to (i) the metastable nature of the AM microstructure and elemental segregations, which result in the formation of highly stable carbides during spheroidizing and austenitization, given that the initial solidification structure strongly influences the heat-treated one [22]; and (ii) the surface-to-volume ratio of the precipitated carbides, as large carbides (~300 nm, *cf.* Figs. 6–3c) may resist dissolution [38]. XRD analysis (*cf.* Fig. 3) confirmed the stability of $M_{23}C_6$ carbides throughout austenitization. This is consistent with findings of Kang et al. [46], who reported that undissolved carbides promote a fine-grained microstructure after quenching.

The stable $M_{23}C_6$ carbides underwent limited growth during subsequent tempering, with an average circular diameter of 340 nm after all heat treatment steps. Supplementary elemental maps (Suppl. Fig. 6) revealed that Cr is partially substituted by Mn, Mo, and V, also strong carbide forming elements [50]. This confirms that $(Cr,Mn,Mo,V)_{23}C_6$ carbides are the main carbide phase present from spheroidizing to the end of tempering. Furthermore, from the first tempered condition onwards, evidence of $Fe_{2-3}C$ carbides, which typically form during tempering [61], can be found in TEM analysis. They are indicated by enrichments of Fe (*cf.* Figs. 6–5b–7b) – besides the Fe-depletion due to $M_{23}C_6$ formation – accompanied by C enrichments, best visible in Figs. 6–7d – 7d. Although no $Fe_{2-3}C$ carbide peaks could be found via XRD during tempering, they may overlap with $M_{23}C_6$ peaks or their content is beneath the detection limit.

3.3. *Mechanical properties*

Mechanical properties after each heat treatment step were evaluated using Vickers hardness measurements. Results could be correlated with the occurrence of (retained) austenite and carbides, plotted in Fig. 7. The data highlight the influence of heat treatment on the mechanical properties and phase occurrence.

The initial hardness after AM in the as-built condition was the lowest at 403 ± 5 HV10, which corresponds to the highest austenite content and the absence of martensite (Fig. 7). After spheroidizing, a significant increase in hardness to 517 ± 5 HV10 was observed due to the phase transformation from austenite to martensite accompanied by carbide formation (Secs. 3.1 and 3.2). This behavior is unusual for a spheroidized material, as this heat treatment is conventionally performed to achieve a softer microstructure for subsequent quenching and tempering [4]. However, in the present study, martensite and early carbide formation during spheroidizing raised the hardness instead of softening the material. Cr segregation in the initial as-built microstructure promoted early carbide formation during spheroidizing, thereby offsetting the conventional softening effect of the spheroidizing treatment. Despite this abnormal hardening phenomenon in the spheroidized condition, the spheroidizing step was crucial for achieving a more homogeneous microstructure after the full heat treatment regime, as can be seen in the optical micrographs presented in Suppl. Fig. 7. This finding aligns with Tóth et al. [3], who reported that spheroidizing enhances microstructural uniformity and thus is crucial to the performance of the final part.

During austenitization and quenching, the hardness increased further to 563 ± 12 HV10 (Fig. 7), corresponding to the presence of martensite and the highest carbide content observed across the heat treatment steps (*cf.* Fig. 5). The higher standard deviation in hardness values is likely due to local phase gradients with more (retained) austenitic and more martensitic areas inside the sample.

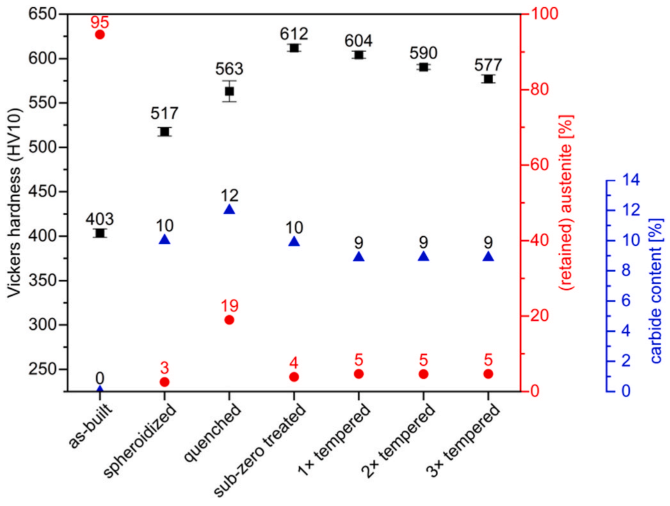

Fig. 7. Correlation between Vickers hardness (HV10) and the fractions of (retained) austenite and carbides in the investigated tool steel after each heat treatment step.

Sub-zero treatment after austenitization successfully transformed most of the retained austenite into martensite, resulting in a substantial increase in hardness to 612 ± 4 HV10 (Fig. 7). Given the high hardness and brittleness associated with martensite, tempering was employed to produce a tougher martensitic phase [4,62].

Following the first tempering step, the retained austenite content exhibited a slight increase from 4 % to 5 %, accompanied by a minor reduction in carbide content from 10 % to 9 % and a hardness value of 604 ± 4 HV10 (Fig. 7). Further tempering steps did not alter the retained austenite or carbide content, indicating that the subsequent reduction in hardness to 577 ± 5 HV10 by the end of tempering was due to stress relaxation and the transformation of bct martensite into bcc martensite (tempered martensite) [46]. No secondary hardening effects were observed, as no new secondary carbides formed during tempering (*cf.* Fig. 4). The final hardness of 577 ± 5 HV10 falls within the range of hardness values reported for heat-treated tool steels in the literature [30, 62,63].

Overall, a clear correlation between microstructural features, phase occurrence and observed variations in hardness is presented. Similar correlations were found by Hoseiny et al. [64] for a hot-rolled and heat-treated modified AISI P20 steel. Throughout the heat treatment process, hardness changes were strongly correlated to the amounts of (retained) austenite and (tempered) martensite, while the carbide content remained relatively constant at ~10 % from spheroidizing to the end of tempering. The volume fraction of retained austenite and (fine and homogeneously distributed) carbides within the matrix plays a critical role in determining the tool steel's properties, including hardness, wear resistance, and corrosion resistance [4]. Retained austenite, known (i) to reduce the hardness of tool steels [65], and (ii) to be metastable with a high probability for (bct) martensite transformation accompanied by volume expansion is therefore undesirable in heat-treated tool steels [42,63].

4. Conclusion

This study examined the microstructural evolution of an additively manufactured (AM) martensitic Cr tool steel and its impact on the mechanical properties across various heat treatment steps using advanced characterization techniques. The studied tool steel demonstrated excellent suitability for laser beam powder bed fusion, as no defects such as cracks, lack-of-fusion voids, or keyhole pores were observed, eliminating the need for post-printing stress relief or hot isostatic pressing.

Nevertheless, to achieve a predominantly martensitic microstructure and the desired mechanical properties, post-processing in form of a tailored multi-step heat treatment regime comprising spheroidizing, austenitization and quenching, sub-zero treatment, and three tempering steps was applied. The heat treatment process was monitored using *in situ* synchrotron X-ray diffraction, enabling real-time tracking of phase transformation. Complementary microstructural analyses and hardness measurements provided detailed correlations between the evolving phase composition and the resulting mechanical properties. Moreover, transition temperatures, and the suitability of the applied heating and cooling rates as well as holding times and temperatures could be determined.

Starting from a predominantly austenitic as-built microstructure with minor δ-ferrite, the alloy transformed into a martensitic microstructure featuring approximately 80 % martensite, 9 % Cr-rich $M_{23}C_6$ carbides, 6 % δ-ferrite and 5 % retained austenite at the end of the whole heat treatment. Cr was substituted by Mo, Mn and V in the $M_{23}C_6$ carbides. The final hardness reached 577 ± 5 HV10, primarily influenced by (retained) austenite and (tempered) martensite content. The initial AM microstructure significantly influenced the heat treatment response, as evidenced by early carbide formation during spheroidizing, attributed to Cr segregations in the as-built condition, and the persistence of the δ-ferritic phase, formed through austenite by-passing during the printing process.

These findings underscore the importance of tailored heat treatment regimes and highlight the necessity for specific adaptations when applied to AM tool steels. By fine-tuning heat treatment parameters, phase evolution, microstructure and mechanical properties can be effectively controlled, demonstrating the importance of post-printing heat treatments in achieving application-specific performance. Furthermore, this study highlighted the value of *in situ* synchrotron X-ray diffraction as a powerful tool for characterizing tool steels and understanding their heat treatment responses.

CRediT authorship contribution statement

N. Ofner: Methodology, conception, Investigation, data evaluation + interpretation, Writing – original draft, Visualization, Writing – review & editing. M. Meindlhumer: Supervision, Writing – original draft, Visualization, Writing – review & editing. P. Kunnas: Investigation, data evaluation + interpretation. A. Asci: Investigation. M. Gocnik: Investigation, data evaluation. A. Stark: Investigation, data evaluation + interpretation. P. Höbenreich: sample fabrication and preparation C. Aumayr: Resources, Project administration, Writing – review & editing. L. Wu: experimental setup and process development. C. Turk: Resources, Methodology, conception, Project administration, Writing – review & editing. J. Keckes: Supervision, Project administration, Writing – original draft, Visualization, Writing – review & editing. S.C. Bodner: Supervision, Methodology, data interpretation, Writing – original draft, Visualization, Writing – review & editing.

Data availability statement

Data will be made available upon reasonable request.

Declaration of competing interest

The authors declare that they have no known competing financial interests or personal relationships that could have appeared to influence the work reported in this paper.

Acknowledgment

The support of Melissa Suschetz and Marco Reiter in sample preparation is gratefully acknowledged. M. M. gratefully acknowledges the financial support by the Austrian Federal Ministry for Labour and Economy, and the Christian Doppler Research Association. We further acknowledge DESY (Hamburg, Germany), a member of the Helmholtz Association HGF, for the provision of experimental facilities. Parts of this research were carried out at PETRA III and we would like to thank Andreas Stark for assistance in using the DIL 805 dilatometer at P07B.

Appendix A. Supplementary data

Supplementary data to this article can be found online at https://doi.org/10.1016/j.jmrt.2025.06.115.

References

[1] Rafael A. Mesquita, tool steels: properties and performance. first ed. CRC Press; 2016.
[2] Højerslev C. Tool steels. Risø National Laboratory; 2001.
[3] Tóth L. Effect of heat treatment on the properties of tool steel. Acta Materialia Transylvanica 2023;6:114–20.
[4] Barlow LD, Du Toit M. Effect of austenitizing heat treatment on the microstructure and hardness of martensitic stainless steel AISI 420. J Mater Eng Perform 2012;21:1327–36.
[5] Zanni Mattia, Berto Filippo, Erik Vullum Per, Tonelli Lavinia, Morri Alessandro, Ceschini Lorella. Effect of heat treatment and defects on the tensile behavior of a hot work tool steel manufactured by laser powder bed fusion. Fatig Fract Eng Mater Struct 2023;46:2681–96.
[6] Deirmina Faraz, Pellizzari Massimo, AlMangour Bandar, Grzesiak Dariusz. Dilatometry study of the heat treatment of a hot work tool steel fabricated by additive manufacturing. Euro PM2019 proceedings. 2019.
[7] Alnajjar M, Christien F, Wolski K, Bosch C. Evidence of austenite by-passing in a stainless steel obtained from laser melting additive manufacturing. Addit Manuf 2019;25:187–95.
[8] García-Hernández C, Naranjo JA, Castro-Sastre MÁ, Berges C, Fernandez-Abia AI, Martín-Pedrosa F, Herranz G, et al. Enhancing wear performance: a comparative study of traditional vs. additive manufacturing techniques for 17–4pH SS. Wear 2024;540–541:205258.
[9] Clausen B, Brown DW, Carpenter JS, Clarke KD, Clarke AJ, Vogel SC, Bernardin JD, et al. Deformation behavior of additively manufactured GP1 stainless steel. Mater Sci Eng, A 2017;696:331–40.
[10] Bajaj P, Hariharan A, Kini A, Kürnsteiner P, Raabe D, Jägle EA. Steels in additive manufacturing: a review of their microstructure and properties. Mater Sci Eng, A 2020;772:138633.
[11] Ofner N, Bodner SC, Kunnas P, Asci A, Kutleša K, Stark A, Höbenreich P, et al. Influence of increasing chromium content on additively manufactured tool steels: microstructural and mechanical evolution before and after heat treatment. J Mater Res Technol 2025;34:2715–27.
[12] Narasimharaju SR, Zeng W, See TL, Zhu Z, Scott P, Jiang X, Lou S. A comprehensive review on laser powder bed fusion of steels: processing, microstructure, defects and control methods, mechanical properties, current challenges and future trends. J Manuf Process 2022;75:375–414.
[13] Ofner N, Bodner SC, Meindlhumer M, Asci A, Kutleša K, Höbenreich P, Aumayr C, et al. Additive manufacturing of a crack-free tool steel with high C and Cr contents: microstructure and mechanical properties. Mater Char 2025;223:114919.
[14] Krakhmalev P, Yadroitsava I, Fredriksson G, Yadroitsev I. In situ heat treatment in selective laser melted martensitic AISI 420 stainless steels. Mater Des 2015;87:380–5.
[15] Malakizadi A, Mallipeddi D, Dadbakhsh S, M'Saoubi R, Krajnik P. Post-processing of additively manufactured metallic alloys – a review. Int J Mach Tool Manufact 2022;179:103908.
[16] Ling C, Li Q, Zhang Z, Yang Y, Zhou W, Chen W, Dong Z, et al. Influence of heat treatment on microstructure, mechanical and corrosion behavior of WE43 alloy fabricated by laser-beam powder bed fusion. Int J Extrem Manuf 2024;6:15001.
[17] Vahedi Nemani A, Ghaffari M, Salahi S, Nasiri A. Effects of post-printing heat treatment on the microstructure and mechanical properties of a wire arc additive manufactured 420 martensitic stainless steel part. Mater Sci Eng, A 2021;813:141167.
[18] Fonseca EB, Gabriel AH, Araújo LC, Santos PL, Campo KN, Lopes ES. Assessment of laser power and scan speed influence on microstructural features and consolidation of AISI H13 tool steel processed by additive manufacturing. Addit Manuf 2020;34:101250.
[19] Yang J, Hawkins L, He L, Mahmood S, Song M, Schulze K, Lou X. Intragranular irradiation-assisted stress corrosion cracking (IASCC) of 316L stainless steel made by laser direct energy deposition additive manufacturing: delta ferrite-dislocation channel interaction. J Nucl Mater 2023;577:154305.
[20] Franco-Correa JC, Martínez-Franco E, Alvarado-Orozco JM, Cáceres-Díaz LA, Espinosa-Arbelaez DG, Villada JA. Effect of conventional heat treatments on the microstructure and microhardness of IN718 obtained by wrought and additive manufacturing. J Mater Eng Perform 2021;30:7035–45.
[21] Philpott W, Jepson MAE, Thomson RC. Comparison of the effects of conventional heat treatments on cast and selective laser melted IN939 alloy. In: Parker J, Shingledecker J, Siefert J, editors. Advances in materials technology for fossil power plants: proceedings from the eighth international conference. ASM International; 2016. p. 735–46.
[22] Pellizzari M, Molinari A. The application-oriented heat treatment of tool steels. Mater Manuf Process 2009;24:723–8.
[23] Seede R, Zhang B, Whitt A, Picak S, Gibbons S, Flater P, Elwany A, et al. Effect of heat treatments on the microstructure and mechanical properties of an ultra-high strength martensitic steel fabricated via laser powder bed fusion additive manufacturing. Addit Manuf 2021;47:102255.
[24] Cheruvathur S, Lass EA, Campbell CE. Additive manufacturing of 17-4 PH stainless steel: post processing heat treatment to achieve uniform reproducible microstructure. J Occup Med 2016;68:930–42.
[25] Vahedi Nemani Alireza, Ghaffari Mahya, Nasiri Ali. On the post-printing heat treatment of a wire arc additively manufactured ER70S part. Materials 2020;13:2795.
[26] Vilardell AM, Hosseini SB, Åsberg M, Dahl-Jendelin A, Krakhmalev P, Oikonomou C, Hatami S. Evaluation of post-treatments of novel hot-work tool steel manufactured by laser powder bed fusion for aluminum die casting applications. Mater Sci Eng, A 2020;800:140305.
[27] Meredith SD, Zuback JS, Keist JS, Palmer TA. Impact of composition on the heat treatment response of additively manufactured 17–4 PH grade stainless steel. Mater Sci Eng, A 2018;738:44–56.
[28] Sun Y, Hebert RJ, Aindow M. Effect of heat treatments on microstructural evolution of additively manufactured and wrought 17-4PH stainless steel. Mater Des 2018;156:429–40.
[29] Åsberg M, Fredriksson G, Hatami S, Fredriksson W, Krakhmalev P. Influence of post treatment on microstructure, porosity and mechanical properties of additive manufactured H13 tool steel. Mater Sci Eng, A 2019;742:584–9.

[30] Law WK, Wong K-C, Wang H, Sun Z, Lim CS. Microstructure evolution in additively manufactured steel molds: a review. J Mater Eng Perform 2021;30:6389–405.

[31] Carasi G, Yu B, Hutten E, Zurob H, Casati R, Vedani M. Effect of heat treatment on microstructure evolution of X38CrMoV5-1 hot-work tool steel produced by L-PBF. Metall Mater Trans A 2021;52:2564–75.

[32] Bae Kichang, Moon Hyoung-Seok, Park Yongho, Jo Ilguk, Lee Junghoon. Influence of tempering temperature and time on microstructure and mechanical properties of additively manufactured H13 tool steel. Materials 2022;15:8329.

[33] Chao Q, Thomas S, Birbilis N, Cizek P, Hodgson PD, Fabijanic D. The effect of post-processing heat treatment on the microstructure, residual stress and mechanical properties of selective laser melted 316L stainless steel. Mater Sci Eng, A 2021;821:141611.

[34] Krell J, Röttger A, Geenen K, Theisen W. General investigations on processing tool steel X40CrMoV5-1 with selective laser melting. J Mater Process Technol 2018;255:679–88.

[35] Kieffer J, Wright JP. PyFAI: a Python library for high performance azimuthal integration on GPU. Powder Diffr 2013;28:S339–50.

[36] Doebelin N, Kleeberg R. Profex: a graphical user interface for the Rietveld refinement program BGMN. Appl Crystall 2015;48:1573–80.

[37] Petzow Günter, Metallographisches Keramographisches. Plastographisches ätzen. Stuttgart, Germany: Schweizerbart Science Publishers; 2024.

[38] Nurbanasari M, Tsakiropoulos P, Palmiere EJ. Microstructural evolution of a heat-treated H23 tool steel. Int J Miner Metall Mater 2015;22:272–84.

[39] Saeidi K, Gao X, Lofaj F, Kvetková L, Shen ZJ. Transformation of austenite to duplex austenite-ferrite assembly in annealed stainless steel 316L consolidated by laser melting. J Alloys Compd 2015;633:463–9.

[40] Oñoro J. Weld metal microstructure analysis of 9–12% Cr steels. Int J Pres Ves Pip 2006;83:540–5.

[41] Ławrynowicz Z. Bainite transformation in experimental Fe-Cr-Mo-V-Ti-C steel. Adv Mater Sci 2013;13:12–8.

[42] Deirmina F, Peghini N, AlMangour B, Grzesiak D, Pellizzari M. Heat treatment and properties of a hot work tool steel fabricated by additive manufacturing. Mater Sci Eng, A 2019;753:109–21.

[43] Bhadeshia HKDH, Honeycombe RWK. Steels: microstructure and properties. Amsterdam: Butterworth-Heinemann; 2017.

[44] Mayr P, Palmer TA, Elmer JW, Specht ED, Allen SM. Formation of delta ferrite in 9 Wt pct Cr steel investigated by in-situ X-ray diffraction using synchrotron radiation. Metall Mater Trans A 2010;41:2462–5.

[45] Nigon GN, Burkan Isgor O, Pasebani S. The effect of annealing on the selective laser melting of 2205 duplex stainless steel: microstructure, grain orientation, and manufacturing challenges. Opt Laser Technol 2021;134:106643.

[46] Kang M, Park G, Jung J-G, Kim B-H, Lee Y-K. The effects of annealing temperature and cooling rate on carbide precipitation behavior in H13 hot-work tool steel. J Alloys Compd 2015;627:359–66.

[47] Honeycombe RWK, Pickering FB. Ferrite and bainite in alloy steels. Metall Trans A 1972;3:1099–112.

[48] Schaeffler AL. Constitution diagram for stainless steel weld metal. 1949.

[49] Guanghua Yan, Huang Xinmin, Yanqing Wang, Xingguo Qin, Ming Yang, Zuoming Chu, Kang Jin. Effects of heat treatment on mechanical properties of H13 steel. Met Sci Heat Treat 2010;52:393–5.

[50] Prudente WR, Lins JFC, S RP, Mendes PSN, Pereira RE. Microstructural evolution under tempering heat treatment in AISI H13 hot-work tool steel. IJERA 2017;7:67–71.

[51] Toby BH. R factors in Rietveld analysis: how good is good enough? Powder Diffr 2006;21:67–70.

[52] Bhambroo R, Roychowdhury S, Kain V, Raja VS. Effect of reverted austenite on mechanical properties of precipitation hardenable 17-4 stainless steel. Mater Sci Eng, A 2013;568:127–33.

[53] Schnitzer R, Radis R, Nöhrer M, Schober M, Hochfellner R, Zinner S, Povoden-Karadeniz E, et al. Reverted austenite in PH 13-8 Mo maraging steels. Mater Chem Phys 2010;122:138–45.

[54] Niessen F, Grumsen FB, Hald J, Somers MAJ. Formation and stabilization of reverted austenite in supermartensitic stainless steel. Metall Res Technol 2018;115:402.

[55] Bish DL, Howard SA. Quantitative phase analysis using the Rietveld method. J Appl Crystallogr 1988;21:86–91.

[56] Zeng YP, Yang W. Effect of heat treatment on the microstructure and hardness of a newly developed plastic injection mold steel. AMM 2013;302:263–8.

[57] Haghdadi N, Laleh M, Moyle M, Primig S. Additive manufacturing of steels: a review of achievements and challenges. J Mater Sci 2021;56:64–107.

[58] Astafurov S, Astafurova E. Phase composition of austenitic stainless steels in additive manufacturing: a review. Metals 2021;11:1052.

[59] Lin M, Zhao X, Han L, Liu Q, Gu J. Microstructural evolution and carbide precipitation in a heat-treated H13 hot work mold steel. Metallogr Microstruct Anal 2016;5:520–7.

[60] Liu H, Fu P, Liu H, Sun C, Ma X, Li D. Microstructure evolution and mechanical properties in 718H pre-hardened mold steel during tempering. Mater Sci Eng, A 2018;709:181–92.

[61] Forsik SA, Rivera-Diaz-del-Castillo PE. Martensitic steels: epsilon carbides in tempered. In: Colás R, Totten GE, editors. Encyclopedia of iron, steel, and their alloys. CRC Press; 2016. p. 2169–81.

[62] Schneider R, Perko J, Reithofer G. Heat treatment of corrosion resistant tool steels for plastic moulding. Mater Manuf Process 2009;24:903–8.

[63] Podgornik B, Puš G, Žužek B, Leskovšek V, Godec M. Heat treatment optimization and properties correlation for H11-type hot-work tool steel. Metall Mater Trans A 2018;49:455–62.

[64] Hoseiny H, Caballero FG, M'Saoubi R, Högman B, Weidow J, Andrén H-O. The influence of heat treatment on the microstructure and machinability of a prehardened mold steel. Metall Mater Trans A 2015;46:2157–71.

[65] Hill H, Raab U, Weber S, Theisen W, Wollmann M, Wagner L. Influence of heat treatment on the performance characteristics of a plastic mold steel. Steel Res Int 2011;82:1290–6.